

EDDY ENERGETICS OF THE SOUTHERN HEMISPHERE OF MARS FROM THE MARS ANALYSIS CORRECTION DATA ASSIMILATION (MACDA).

J. Michael Battalio, Istvan Szunyogh, Mark Lemmon, *Department of Atmospheric Science, Texas A&M University (battalio@tamu.edu).*

1 Introduction

Transient, baroclinic eddies are ubiquitous on Mars in both hemispheres, but waves in the southern hemisphere have received limited interest (Hinson and Wilson, 2002; Banfield et al., 2004) because they are weaker than their northern hemisphere counterparts and because there are no in situ measurements close to the southern hemisphere midlatitudes. To allow for the direct comparison of the eddies in each hemisphere, we investigate the energetics of the transient waves in the southern hemisphere.

The eddy energetics of the northern hemisphere of Mars have been studied in great detail. Waves in the northern hemisphere act like those of Earth as they are initiated via geopotential flux convergence, grow through baroclinic energy conversion, and decay through barotropic energy conversion and dissipation (Kavulich et al., 2013). The Planitias have the highest levels of eddy kinetic energy (EKE) and baroclinic energy conversion, and barotropic energy conversion removes EKE by converting it to energy of the mean flow on the downstream side of high topography like Tharsis or Arabia Terra. Battalio et al. (2016) examined the energetics of transient waves in the northern hemisphere before the winter solstice ($L_s = 200^\circ - 230^\circ$) for three years to compare eddies occurring during the 2001 global-scale dust storm during MY25 to two non-global-scale dust storm years. Eddies occurring in MY24 or MY26 were similar to those in Kavulich et al. (2013), but waves during the global-scale dust storm gained a relatively larger part of their EKE from barotropic energy conversion, because baroclinic energy conversion was somewhat suppressed as a result of the more stable mean-state of the atmosphere due to high dust opacities.

Baroclinic waves in the southern hemisphere are favored between autumn and spring with a lull in activity around winter solstice (Mooring and Wilson, 2015). Waves are strongest between $L_s = 15^\circ - 60^\circ$, then abruptly cease between $L_s = 70^\circ - 110^\circ$, and resume after $L_s = 120^\circ$ (Lewis et al., 2016). The waves are weaker than those in the northern hemisphere mostly due to the zonally asymmetric topography (Mulholland et al., 2016). The solstitial pause in activity is primarily due to stabilization of the atmosphere by midlevel polar warming (Kuroda et al., 2007) and the migration of the baroclinic wave guide to latitudes with asymmetric zonal topography and with some effect from a barotropic governor (Mulholland et al., 2016).

2 Methods

We use the Mars Analysis Correction Data Assimilation (MACDA) (v1.0) (Montabone et al., 2014) for the inves-

tigation of the eddy energetics of southern hemisphere waves. MACDA is a reanalysis of Thermal Emission Spectrometer retrievals (Smith, 2004) of dust opacities and thermal profiles that are assimilated into the UK version of the LMD MGCM (Forget et al., 1999). MACDA is 5° by 5° resolution at 25 sigma levels every two Mars hours.

The eddy kinetic energy equation of Orlandi and Katzfey (1991) is used to describe the energetics:

$$\frac{\partial}{\partial t} \langle K_e \rangle = \overbrace{-\langle \nabla_3 \cdot \mathbf{v}_3 K_e \rangle}^1 - \overbrace{\langle \nabla_3 \cdot \mathbf{v}'_3 \phi' \rangle}^2 - \overbrace{\langle \omega' \alpha' \rangle}^3 - \overbrace{\langle \mathbf{v}' \cdot (\mathbf{v}'_3 \cdot \nabla_3) \mathbf{v}_m - \mathbf{v}' \cdot (\mathbf{v}'_3 \cdot \nabla_3) \mathbf{v}' \rangle}^4 + \overbrace{\langle (Residue) \rangle}^5, \quad (1)$$

where the kinetic energy per unit mass is $K_e = \frac{1}{2}(u'^2 + v'^2)$. Eddy quantities are indicated with primes and defined as perturbations from the time-mean flow (denoted with subscripted m). Angle brackets indicate vertical averaging in pressure coordinates. The overbar denotes terms that are time averaged. The geopotential height is ϕ , and $\alpha = 1/\rho$ is the specific volume.

The meanings of the terms are as follows: term 1 is the EKE advection; term 2 is the geopotential flux convergence (GFC); term 3 is the baroclinic energy conversion (BCEC); term 4 is the barotropic energy conversion (BTEC); and term 5 is the residual, which contains effects not explicitly accounted for, such as diabatic effects, friction, dissipation, or interpolation errors. The residual is found by calculating the left-hand side and subtracting the right-hand side terms.

The eddy components are defined from a 30-Sol running mean, and a Hamming-window filter is used to remove eddies with frequency of $0.95 - 1.05 \text{ Sol}^{-1}$ or frequency higher than 1.82 Sol^{-1} . The vertical velocities are calculated using the quasi-geostrophic ω equation as in Battalio et al. (2016).

3 Preliminary Results

Three time periods are covered in the analysis: pre-solstice ($L_s = 20^\circ - 50^\circ$), solstice ($L_s = 75^\circ - 105^\circ$), and post-solstice ($L_s = 150^\circ - 180^\circ$). Spans are limited to $L_s = 30^\circ$ to avoid periods where TES retrievals were unavailable and the MGCM produced analyses unconstrained by observed information. The pre-solstice period is averaged from MY 25, MY 26, and MY 27. The solstice period contains only MY 25 and MY 26, and the post-solstice period contains only MY 24 and MY 26 due to a large observation gap during the initiation of the global-scale dust storm during MY 25.

3.1 Pressure-weighted averages

The pressure-weighted fields for each of the EKE equation terms are shown in Fig. 1. The pre-solstice is on the left; solstice is in the middle; post-solstice is on the right. In order, from top to bottom, the rows are: EKE, BCEC, GFC, EKE advection, BTEC, and the residue.

The eddy kinetic energy shows great variability between the time periods. In the pre-solstice period there is a small region just upstream of Hellas and a broad ‘C’-shaped area over Tharsis to the west of Argyre and then curving back to the west and north. There is no semicontinuous band of EKE as was found in Kavulich et al. (2013) or Battalio et al. (2016) in the northern hemisphere. EKE during the solstice period is substantially reduced from the pre-solstice period but still has large values over Tharsis; however, all other activity is north of 50° S. The spatial distribution of the EKE of the post-solstice period is the most similar to that in the northern hemisphere (Battalio et al., 2016). There is one area of EKE just upstream and slightly southwest of Argyre, and another, weaker area to the southwest of Hellas. (Note the change in the magnitude of the color scale for the post-solstice season.) The large area of EKE over Tharsis is not present in the post-solstice period. In all seasons, the impact basins are local minima of EKE. The BCEC (Fig. 1 second row) shows somewhat less seasonal variability compared to the EKE. The highest area of BCEC in each season is found south of Tharsis around 60° S and upstream of Argyre between 150° E to 300° E. The post-solstice period has by far the strongest BCEC, with the solstice period containing the weakest BCEC. Also in the pre- and post-solstice periods there is a second local maximum of BCEC upstream of Hellas, but it is substantially weaker than the maximum upstream of Argyre. In the solstice period there is an area of negative BCEC that is mirrored on the eastern side of Hellas as well. This negative area on the eastern side of Hellas is present in the pre-solstice season as well. The distribution of BCEC around Hellas is related to the counter-clockwise motion of eddies within the basin (Mooring and Wilson, 2015).

The GFC (Fig. 1 third row) is much more variable than the BCEC. The strongest area is on the southeastern side of Hellas in all three seasons, but in the pre- and post-solstice seasons there is an area of geopotential flux divergence. The EKE advection term (Fig. 1 fourth row) has a smaller magnitude than the GFC term but is generally negative southwest of Tharsis and positive upstream of Argyre and downstream of Hellas. The high wavenumber pattern to the GFC and advection terms is due to large interannual variability in these terms (not shown) so that no one area of GFC or advection is present in all years. We attribute these changes to variability in eddy strength and track across years.

The BTEC term (Fig. 1 fifth row) has a strong negative region on the western side of Argyre in each period. Each period also has positive BTEC on the southeastern side of Hellas. The pre- and post-solstice periods have positive BTEC on the southwestern side of Tharsis as well. The solstice period has negative BTEC everywhere except the aforementioned region near Hellas, which follows the finding by Lewis et al. (2016) that barotropic

instability increases during the winter season. Negative BTEC associated with topography is similar to what was found in the northern hemisphere where eddies traveling around topography lose energy to the mean flow (Kavulich et al., 2013; Battalio et al., 2016).

Finally, the residue term is highly variable between the periods (Fig. 1 bottom row). In the solstice period, there are large positive regions especially in the southwestern part of Hellas and throughout the periphery of the basin. There are also local positive maxima of the residue around Tharsis during the solstice season. This is in contrast to the post-solstice season that has a majority negative residue, especially over the impact basins. The pre-solstice period is somewhat in between the post-solstice and solstice periods with negative residue south of Tharsis and a couplet of positive and negative residue in Hellas. The widespread areas of negative residue in the pre- and post-solstice seasons are consistent with the northern hemisphere and with both hemispheres of Earth. The large negative values are attributed to dissipation and friction acting to remove EKE from the eddies. This particularly appears to be the case as the negative areas are near topography. The large positive values of the residue during the solstice period seem to suggest strong diabatic effects contributing to the EKE as friction or dissipation cannot have a positive contribution to the EKE, and there is no obvious source of errors in the model or data assimilation that should only occur during the solstice period.

3.2 Inter-annual variability

There is large interannual variability between years for each period. This is shown in Fig. 2, which shows the integrated, pressure-weighted terms of the EKE equation. MY 25 has a larger average of EKE and BCEC in the pre-solstice period than either MY 26 or 27 and larger peaks of EKE. This could be due to the run up of the global-scale dust storm in MY 25. The advection, GFC, BTEC terms are all comparable in intensity between each year before $L_s = 120^\circ$. The dataset ends before the solstice period begins in MY 27, but lower energetics begin at around the same time ($L_s = 60^\circ$) in both MY 25 and 26. With only a couple of exceptions, the terms remain low and of the same order of magnitude in both years during the solsticial pause. However, MY 26 resumes activity approximately $L_s = 20^\circ$ sooner than MY 25. Once MY 25 activity resumes, it has the strongest EKE with the exception of one eddy during MY 24. For MY 25, we attribute the stronger, longer-duration EKE activity to the 2001 global-scale dust storm that formed in the southern hemisphere at this time. Interestingly, the global-scale dust storm does not seem to substantially increase the advection, GFC or BTEC terms above that of other years, but the BCEC appears to be the strongest in MY 25 post-solstice. MY 26 has activity that is weaker than MY 24 or 25, but its post-solstice is still stronger than any pre-solstice season. MY 24 has several strong EKE events, but its background level of EKE is about the same as that during post-solstice in MY 26.

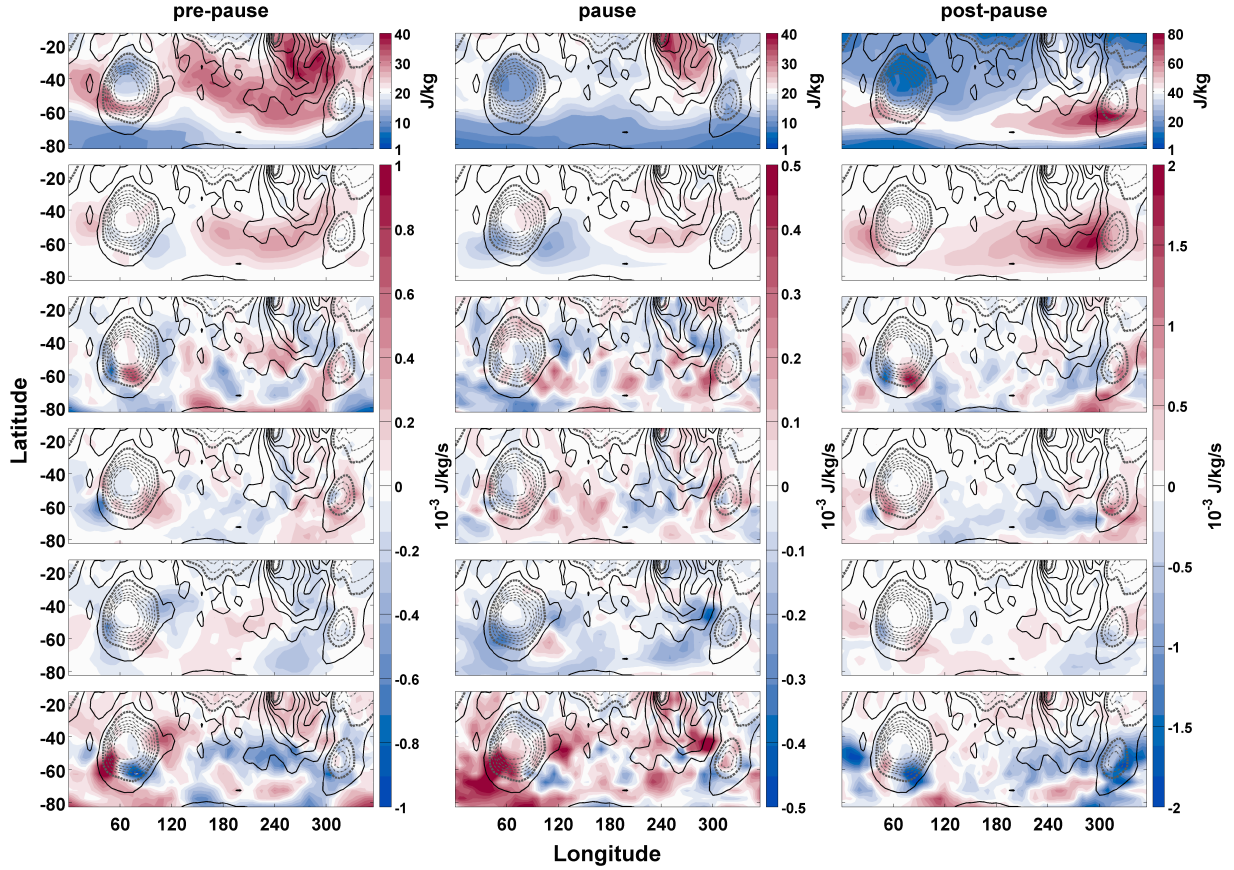


Figure 1: Time-mean, pressure-weighted vertical averages of the terms in the eddy kinetic energy equation for the seasonal average of $L_s = 20^\circ - 50^\circ$ for MY 25, MY26, and MY 27 (left column), of $L_s = 75^\circ - 105^\circ$ for MY 25 and MY26 (middle column), and $L_s = 150^\circ - 180^\circ$ for MY 24 (starting at $L_s = 153.7^\circ$) and MY 26 (left column). Shown is the eddy kinetic energy (top), baroclinic energy conversion (second row), geopotential flux convergence (third row), the eddy kinetic energy transport (fourth row), the barotropic energy conversion (fifth row), and the residue (bottom). Contours are surface elevation in 1000 m increments with dashed values below mean geoid and the 0 mean geoid in bold.

4 Continuing Work

Battalio et al. (2016) concentrated on the northern hemisphere pre-winter-solstice period of eddy activity to allow for comparison to Kavulich et al. (2013). Work presented here has focused on the southern hemisphere. Continuing work will focus on three facets of the energetics. One, the analysis done in the southern hemisphere will be extended to investigate the differences, if any, in individual waves during each of the three eddy seasons and to attempt to explain the larger magnitude of energetics during the post-solstice season compared to pre-solstice. Two, a similar investigation of the post-solstice waves in the northern hemisphere will be undertaken to compare to the work of Battalio et al. (2016) in the pre-solstice time. Finally, the energetics of each season in the southern and northern hemispheres will be spectrally decomposed by zonal wavenumber to ascertain the influence of differing sizes of disturbance to the average energetics and what, if any, influence stationary waves have on energetics during the solsticial pause.

References

- Banfield, D., B. Conrath, P. Gierasch, R. Wilson, and M. Smith, 2004: Traveling waves in the martian atmosphere from MGS TES Nadir data. *Icarus*, **170** (2), 365–403, doi:10.1016/j.icarus.2004.03.015.
- Battalio, M., I. Szunyogh, and M. Lemmon, 2016: Energetics of the martian atmosphere using the Mars Analysis Correction Data Assimilation (MACDA) dataset. *Icarus*, **276**, 1–20, doi:10.1016/j.actamat.2015.02.029.
- Forget, F., et al., 1999: Improved general circulation models of the Martian atmosphere from the surface to above 80 km. *Journal of Geophysical Research*, **104** (E10), 24 155, doi:10.1029/1999JE001025.
- Hinson, D. P. and R. J. Wilson, 2002: Transient eddies in the southern hemisphere of Mars. *Geophysical Research Letters*, **29** (7), 3–6, doi:10.1029/2001GL014103.
- Kavulich, M. J., I. Szunyogh, G. Gyarmati, and R. J. Wilson, 2013: Local Dynamics of Baroclinic Waves in the Martian

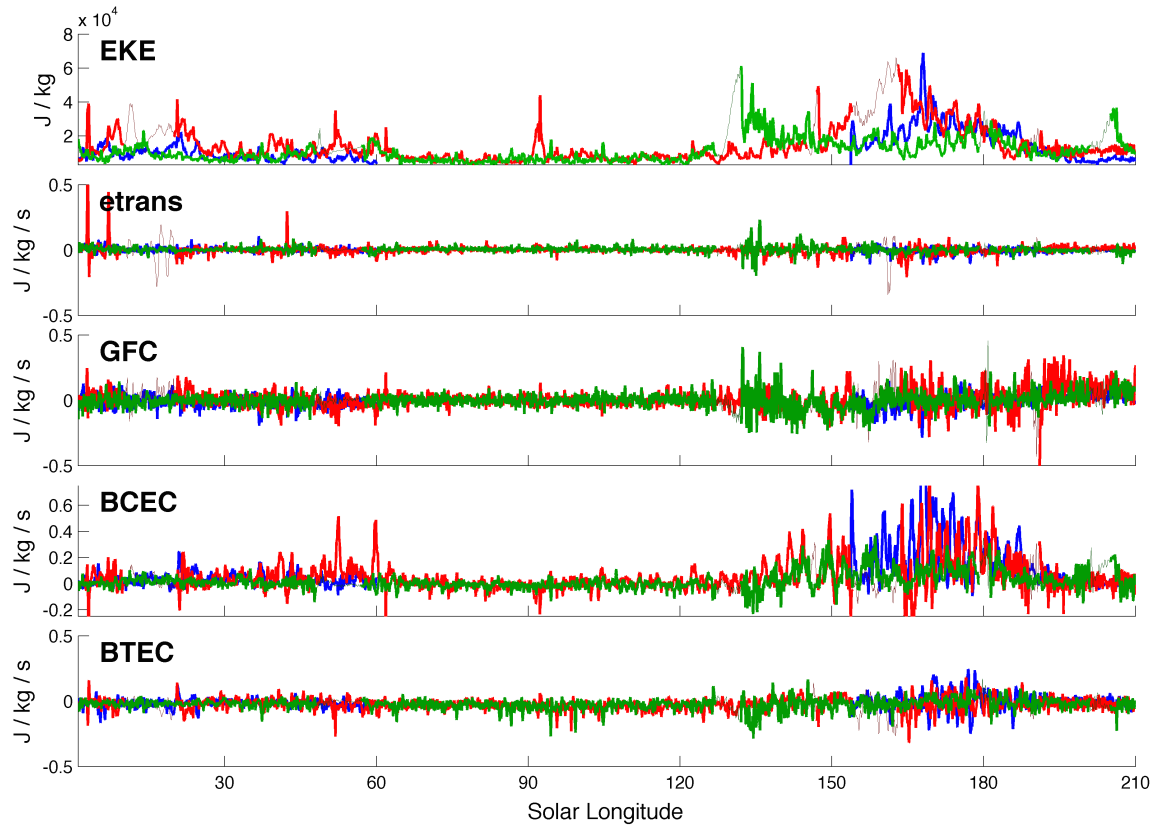


Figure 2: Summed, pressure-weighted EKE equation terms in the $57.5^\circ - 82.5^\circ$ S band for MY27 ($L_s = 20^\circ - 60^\circ$) and MY 24 ($L_s = 153.7^\circ - 180^\circ$) in blue, MY 25 in red, and MY 26 in green. Times longer in duration than $L_s = 1^\circ$ when TES retrievals were unavailable and the MACDA GCM ran freely are shown in thinner lines.

Atmosphere. *Journal of the Atmospheric Sciences*, **70** (11), 3415–3447, doi:10.1175/JAS-D-12-0262.1.

Kuroda, T., A. S. Medvedev, P. Hartogh, and M. Takahashi, 2007: Seasonal changes of the baroclinic wave activity in the northern hemisphere of Mars simulated with a GCM. *Geophysical Research Letters*, **34** (9), L09 203, doi: 10.1029/2006GL028816.

Lewis, S. R., D. P. Mulholland, P. L. Read, L. Montabone, R. J. Wilson, and M. D. Smith, 2016: The solstitial pause on Mars: 1. A planetary wave reanalysis. *Icarus*, **264**, 456–464, doi:10.1016/j.icarus.2015.08.039.

Montabone, L., et al., 2014: The Mars Analysis Correction Data Assimilation (MACDA) Dataset V1.0. *Geoscience Data Journal*, **1**, 129–139, doi:10.1002/gdj3.13.

Mooring, T. A. and R. J. Wilson, 2015: Transient eddies in the MACDA Mars reanalysis. *Journal of Geophysical Research: Planets*, **120**, 1–26, doi:10.1002/2015JE004824.

Mulholland, D. P., S. R. Lewis, P. L. Read, J.-B. Madeleine, and F. Forget, 2016: The solstitial pause on Mars: 2 modelling and investigation of causes. *Icarus*, **264**, 465–477, doi:10.1016/j.icarus.2015.08.038.

Orlanski, I. and J. Katzfey, 1991: The Life Cycle of a Cyclone Wave in the Southern Hemisphere. Part I: Eddy Energy Budget. *Journal of the Atmospheric Sciences*, **48** (17), 1973–1998.

Smith, M. D., 2004: Interannual variability in TES atmospheric observations of Mars during 1999–2003. *Icarus*, **167** (1), 148–165, doi:10.1016/j.icarus.2003.09.010.

Wang, H. and A. D. Toigo, 2016: The variability, structure and energy conversion of the northern hemisphere traveling waves simulated in a Mars general circulation model. *Icarus*, **271**, 207–221, doi:10.1016/j.icarus.2016.02.005.